Optimized survey design for Electrical Resistivity Tomography: combined optimization of measurement configuration and electrode placement

Sebastian Uhlemann[1,2,*], Paul B. Wilkinson[1], Hansruedi Maurer[2], Florian M. Wagner[3], Timothy C. Johnson[4], and Jonathan E. Chambers[1]

1 – British Geological Survey, Environmental Science Centre, Keyworth, Nottingham, UK

2 – ETH Zurich, Institute of Geophysics, Zurich, Switzerland

3 – University of Bonn, Steinmann Institute, Department of Geophysics, Bonn, Germany

4 – Pacific Northwest National Laboratory, Richland, USA

Abbreviated title: Optimization of ERT measurement configuration and electrode placement

*Corresponding Author. Email: suhl@bgs.ac.uk, Phone: +44 115 936 3271

32 **SUMMARY**

33 Within geoelectrical imaging, the choice of measurement configurations and electrode
34 locations is known to control the image resolution. Previous work has shown that optimized
35 survey designs can provide a model resolution that is superior to standard survey designs. This
36 paper demonstrates a methodology to optimize resolution within a target area, while limiting
37 the number of required electrodes, thereby selecting optimal electrode locations. This is
38 achieved by extending previous work on the 'Compare-R' algorithm, which by calculating
39 updates to the resolution matrix optimizes the model resolution in a target area. Here, an
40 additional weighting factor is introduced that allows to preferentially adding measurement
41 configurations that can be acquired on a given set of electrodes. The performance of the
42 optimization is tested on two synthetic examples and verified with a laboratory study. The
43 effect of the weighting factor is investigated using an acquisition layout comprising a single
44 line of electrodes. The results show that an increasing weight decreases the area of improved
45 resolution, but leads to a smaller number of electrode positions. Imaging results superior to a
46 standard survey design were achieved using 56 % fewer electrodes. The performance was also
47 tested on a 3D acquisition grid, where superior resolution within a target at the base of an
48 embankment was achieved using 22 % fewer electrodes than a comparable standard survey.
49 The effect of the underlying resistivity distribution on the performance of the optimization was
50 investigated and it was shown that even strong resistivity contrasts only have minor impact.
51 The synthetic results were verified in a laboratory tank experiment, where notable image
52 improvements were achieved. This work shows that optimized surveys can be designed that
53 have a resolution superior to standard survey designs, while requiring significantly fewer
54 electrodes. This methodology thereby provides a means for improving the efficiency of
55 geoelectrical imaging.

56

1 INTRODUCTION

Within the last two decades geoelectrical data acquisition and processing have seen crucial developments. Automatic, multi-channel measurement systems combined with autonomous processing schemes nowadays allow for real-time electrical resistivity tomography (ERT) monitoring (Johnson, 2016; Parsekian et al., 2015; Singha et al., 2014). This has opened the opportunity to study a wide variety of subsurface processes, such as nuclear waste decommissioning (Daily et al., 2004; Johnson et al., 2012; Kuras et al., 2016), CO_2 sequestration (Benisch et al., 2015; Schmidt-Hattenberger et al., 2016), landslide hydrology (Gance et al., 2016; Supper et al., 2014; Uhlemann et al., 2017), permafrost degradation (Hilbich et al., 2008; Krautblatter et al., 2010), and landfill processes (Dumont, 2017; Godio et al., 2015; Grellier et al., 2008). Monitoring studies where data are acquired on hundreds of electrodes within short timescales are becoming more frequent (Kuras et al., 2016; Uhlemann et al., 2017). Nevertheless, the time required for data acquisition, and how to handle and interpret the vast amount of data such installations provide are posing new challenges (Parsekian et al., 2015; Rucker, 2014). To overcome these, efforts are undertaken to limit the amount of data without reducing their information content.

This can be achieved by optimizing the survey design, which can be broadly divided into two approaches. The most common approach is to take a set of electrodes and choose measurement combinations from it that maximises the image resolution (Loke et al., 2013). Those algorithms can achieve an image resolution superior or equal to standard survey designs, e.g. Wenner-Schlumberger or dipole-dipole, with the same or fewer number of measurements (Loke et al., 2014; Stummer et al., 2004; Wilkinson et al., 2012). The other approach is to optimize the sensor positions. Wagner et al. (2015) showed that by using an optimized set of electrode locations the resolution within a target horizon can be significantly improved compared to

83 conventional equally spaced electrode arrays. Both approaches reduce the amount of data while

84 preserving image resolution.

85 Here we present a novel algorithm that combines these two approaches. We extend the

86 methodology introduced by Wilkinson et al. (2015), which optimized measurement

87 configurations to improve image resolution within a target area, by preferentially adding

88 measurement configurations that can be acquired on a given set of electrodes. The new

89 approach is tested on a synthetic example, where measurement configurations and electrode

90 positions are chosen from a linear electrode array, and by a laboratory experiment simulating

91 a 3D measurement setup (i.e. an electrode grid) on an embankment. We show that this

92 methodology can generate an optimal set of electrode locations and measurement

93 configurations that is a fraction of all possible locations and configurations, while still offering

94 equal or superior resolution to standard survey designs. This is in contrast to previous

95 optimisation strategies that solely aimed to improve the model resolution (Loke et al., 2013;

96 Stummer et al., 2004; Wilkinson et al., 2015). The presented approach will not only aid in

97 creating survey designs for optimal resolution of a target area, but also reduce costs for ERT

98 installations, as fewer electrodes and cables will be required for the optimized survey. Hence

99 it addresses exactly what Curtis and Maurer (2000) define as an optimal survey, i.e., a survey

100 that leads to high accuracy and reliability of the model estimates, while being easily realizable

101 under minimal financial effort. Thus, this methodology will aid in improving the efficiency of

102 ERT data acquisition, in particular if *a priori* information about the subsurface is available.

103 While it is applied to an ERT example here, the approach should be easily transferrable to

104 optimizing image resolution for other geophysical tomographic methods.

105 **2 METHODOLOGY**

106   Most recent studies on ERT measurement optimization make use of the model resolution

107   matrix (Alfouzan et al., 2010; Loke et al., 2015b, 2014, 2010; Stummer et al., 2004; Wagner et

108   al., 2015; Wilkinson et al., 2015, 2012, 2006). In comparison to sensitivity based optimization

109   strategies (Athanasiou et al., 2009; Tsakirrbaloglou et al., 2016; Tsourlos et al., 2016), the

110   model resolution accounts for linear (in)dependency between measurement configurations, and

111   is therefore used here as well. The model resolution matrix **R** quantifies how well each model

112   cell of a resistivity image is resolved by the measured data. For the linearized iterative Gauss-

113   Newton solution of the ERT problem, **R** is defined as (Wilkinson et al., 2006):

114                                $$\mathbf{R} = (\mathbf{G}^{\mathrm{T}}\mathbf{G} + \mathbf{C})^{-1}\mathbf{G}^{\mathrm{T}}\mathbf{G},$$ (1)

115   with the Jacobian matrix **G** and the constraint matrix **C**. The main diagonal elements R_j of **R**

116   are referred to here as the model resolution and range between 0 and 1, where $R_j = 0$ represents

117   an entirely unresolved, and $R_j = 1$ a perfectly resolved cell j. Although **C** could represent any

118   kind of model constraints (Loke et al., 2014; Wilkinson et al., 2012), here it is defined as **C** =

119    $\lambda\mathbf{I}$, with **I** being the identity matrix, to represent a simple damped least square problem

120   (Wilkinson et al., 2006). The choice of the damping factor λ is problem specific, with larger

121   values leading to lower resolution (Loke et al., 2010). For this type of optimization problem, λ

122   is often chosen so that the model resolution is small ($R \approx 0.05$) at a certain distance from the

123   electrodes, typically at the base of the model (Stummer et al., 2004; Wilkinson et al., 2006).

124   Note that λ is not only affecting the absolute values of the diagonal elements of **R**, but also the

125   distribution of the relative magnitudes. Nevertheless, Loke et al. (2010) have shown that the

126   relative performance of the optimization is not particularly sensitive to the value of λ.

127   The optimization is an iterative process and starts from a small set of measurements from a

128   small number of electrodes. Additional measurements are selected from a comprehensive set,

129   comprising alpha and beta-type configurations (Loke et al., 2015). For each possible new

measurement, the change in the resolution matrix $\mathbf{\Delta R}$ is calculated using a Sherman-Morrison

Rank-1 update of the resolution matrix, which is defined as (Loke et al., 2014; Wilkinson et

al., 2006):

$$\mathbf{\Delta R_b} = \frac{\mathbf{z}}{1 + (\mathbf{g} \cdot \mathbf{z})} (\mathbf{g^T} - \mathbf{y^T}) \tag{2}$$

where

$$\mathbf{z} = \left(\mathbf{G_b^T G_b} + \mathbf{C}\right)^{-1} \mathbf{g}, \ \mathbf{y} = \left(\mathbf{G_b^T G_b}\right)\mathbf{z}, \tag{3}$$

with the Jacobian matrix $\mathbf{G_b}$ consisting of the sensitivities of the measurements of the current

base set, and $\mathbf{g}$ comprising the sensitivities of the new test configuration. Following Wilkinson

et al. (2015) all additional measurements are ranked according to the calculated improvement

of the resolution in the target region

$$F_{CR} = \frac{1}{m} \sum_{j=1}^{m} \frac{w_{t,j} \Delta R_{b,j}}{R_{c,j}} , \tag{4}$$

with the number of model cells m, the resolution of cell j given by the comprehensive set $R_{c,j}$,

and a weighting factor $w_{t,j}$ that is 1 if cell j is within the target region and 10^{-12} if not. Survey

designs are often "focused" on specific target areas, which requires *a priori* information about

the subsurface properties (Curtis, 1999; Furman et al., 2007; Loke et al., 2015b; Roux and

Garcia, 2014). In order to penalize measurements that would require electrodes other than those

already present in the current base set, the weighting factor w_e was added to equation 4:

$$F_{CR} = \frac{1}{m w_e^\beta} \sum_{j=1}^{m} \frac{w_{t,j} \Delta R_{b,j}}{R_{c,j}} \tag{5}$$

For a given measurement, $w_e = (1 + n_e)$ where n_e is the number of additional electrodes required

(from 0 to 4). This weighting factor is controlled by the exponent β; increasing values of β

150   cause a stronger penalty for measurements requiring additional electrodes. The highest ranked

151   measurement is added to the current base set. The second highest is only added if its linear

152   dependency to the first is below a certain limit. Wilkinson et al. (2012) showed that superior

153   results can be obtained by setting this limit to the value of the current average relative resolution

154   S, defined as

$$S = \frac{1}{n} \sum_{k=1}^{n} \frac{R_{b,k}}{R_{c,k}} \tag{6}$$

156   which was evaluated for all cells k within the target volume. Linearity tests are performed and

157   measurements added until a certain fraction of the size of the current base set have been added,

158   defined by the step size of the iterative optimization process. After each iteration, $\mathbf{R}_b$ is

159   recalculated. Loke et al. (2014) showed that the performance of the optimization degrades with

160   increasing step size, however, computationally larger step sizes are preferable as $\mathbf{R}_b$ needs to

161   be recalculated fewer times; this is further discussed in the following section.

162   Calculations of $\mathbf{G}$, $\mathbf{R}_c$, $\mathbf{R}_b$, and F_{CR} were facilitated by adapting the fully parallelized source

163   code of E4D (Johnson et al., 2010), and exploiting OpenBLAS routines (Wang et al., 2013) to

164   improve computational performance of the $\mathbf{R}$ and F_{CR} calculations. All optimizations presented

165   in this study were calculated on a machine with four Intel® Xeon® E5-2697V3 CPUs,

166   comprising in total 56 cores running at 2.6 GHz. Loke et al. (2015) found that using single

167   precision, compared to double precision, caused only a marginal change in the calculated model

168   resolution, while significantly reducing calculation times. Hence, single precision was used in

169   the calculation of $\mathbf{R}$ and F_{CR}.

170   For N electrodes $N(N-1)(N-2)(N-3)/8$ unique four-point measurements can theoretically be

171   acquired (accounting for polarity and reciprocity); for 32 and 117 electrodes this would equal

172   107 880 and 22 241 115 measurements, respectively. Evaluating all of these measurements

173 would be computationally very demanding and some measurements would be impractical to

174 acquire due to small signal-to-noise ratios and high sensitivities to electrode misplacements.

175 Thus, the comprehensive set from which measurements are added at each iteration comprises

176 only alpha and beta-type configurations that have geometric factors and sensitivities below

177 specified problem-specific limits.

3 LINEAR ELECTRODE ARRAY

179 The methodology was tested first on a simple synthetic model, comprising 32 possible

180 electrode locations spaced by 1 m along a single line. A trapezoidal prism in the centre of the

181 model formed the target volume, within which the resolution was to be optimized (Figure 1).

182 As the methodology was developed for 3D problems, this example was calculated on a 3D

183 representation of a linear electrode array. The model domain was discretized using an

184 unstructured tetrahedral mesh, comprising 3312 elements (equal to the number of model

185 parameters m), which was refined around the electrode locations and extended beyond to

186 account for 'outer-space' sensitivities (Maurer and Friedel, 2006). The comprehensive set

187 comprised alpha and beta-type configurations with a maximum geometric factor $K_{max} = 4146.9$

188 m (equal to a dipole-dipole geometric factor for $a = 1$ and $n = 10$) and a maximum geometric

189 sensitivity of $s/K = 5$ m^{-1} (Wilkinson et al., 2008), totalling 70 555 four-point measurement

190 configurations. A description of the alpha and beta-type arrays can be found in Loke et al.

191 (2015a). Szalai and Szarka (2011) present other possible measurement configurations that

192 could be added to the comprehensive set (e.g. "Null" or "Quasi-null" arrays). However, some

193 of those may cause instabilities in the inversion if the data and model parameters are

194 logarithmically transformed (Johnson et al., 2010), which is desirable due to the large range of

195 resistivities often encountered in geoelectrical imaging. Measurements involving remote

196 electrodes (pole-pole or pole-dipole) could also be included, but often present difficulties in

197 practical site investigations and cannot be used in tank experiments. Restricting the

198   comprehensive set to alpha- and beta-type configurations below a certain limit for their

199   geometric factor removes measurement configurations that are likely to be unstable (Loke et

200   al., 2014). The damping factor $\lambda = 0.004$ was chosen so that the model resolution was small at

201   the base of the model ($R < 0.05$; Wilkinson et al., 2006). The initial measurement set comprised

202   30 measurements employing six electrodes located above the target area.

Fig. 1

203   To investigate the effect of the exponent β, which controls the penalty for including additional

204   electrodes at every iteration, the optimization was run for values of $\beta = 0.0, 2.0$, and 5.0 (Figure

205   2). Each optimization employed a step size of 5%, meaning that at each iteration the number

206   of measurements in the optimized set increased by 5%. Setting $\beta = 0.0$ is equivalent to the

207   methodology introduced by Wilkinson et al. (2015) to optimize resolution within a target

208   region. For $\beta = 0.0$ all possible electrode locations are used once the set includes more than 327

209   measurements, which is reached within the first 49 iterations. This 'unconstrained'

210   optimization yields mostly superior resolution compared to employing larger values of β. For

211    $\beta = 2.0$ all possible electrodes are included in the survey once it comprises 6201 measurements.

212   From this point, the resolution achieved in the optimization is independent of β. Despite using

213   up to 59% fewer electrodes, the relative resolution achieved with $\beta = 2.0$ is similar to $\beta = 0.0$,

214   with differences in average relative resolution being less than 0.06 for all iterations. During a

215   few iterations, i.e., between 386 and 1303 measurements (Figure 2b), the relative resolution

216   obtained with $\beta = 2.0$ is superior to $\beta = 0.0$, with a maximum difference of 0.016. This is likely

217   to be an effect of a localised optimum that was found by constraining the optimization to use a

218   certain set of electrodes. However, once the measurement set comprises more than 1303

219   measurements, the constraints on adding additional electrodes limit the increase in relative

220   resolution compared to $\beta = 0.0$.

Fig. 2

221   Using $\beta = 5.0$, for small measurement sets the optimized survey employs considerably fewer

222   electrodes than $\beta = 0.0$ or 2.0. When the survey comprises about 2750 measurements, $\beta = 0.0$

223   uses all 32 electrodes and $\beta = 2.0$ uses 23 electrodes, while $\beta = 5.0$ uses only 17 electrodes,

224   thus only 53% of the available electrodes. This, however, also results in a relative resolution

225   0.22 smaller than for $\beta = 0.0$. For less than 1500 measurements (Figure 2b), this difference is

226   smaller than 0.09, despite using about 50% fewer electrodes than $\beta = 0.0$. The $\beta = 5.0$ optimized

227   survey includes all possible electrodes once the set comprises more than 15000 measurements.

228   In general, the higher β the longer a certain set of electrodes is used to optimize the resolution,

229   leading to a decreasing performance of the optimization.

230   Figure 2 also shows the relative resolution of a standard survey, comprising 934 dipole-dipole

231   and Wenner-Schlumberger measurements and using all 32 electrodes. This shows the benefit

232   of the presented approach clearly. The optimization, for all tested values of β, achieves a

233   relative resolution in the target area higher than the standard survey ($S = 0.185$). For $\beta = 0.0$,

234   the improvement in the relative resolution is 0.042, for $\beta = 2.0$ it is 0.054 and for $\beta = 5.0$ it is

235   0.018. In the case of $\beta = 2.0$ and $\beta = 5.0$ this improvement is achieved using 43.8% and 56.3%

236   fewer electrodes than used in the standard survey, respectively.

237   Figure 3 shows the resolution within the imaging plane for the standard and optimized surveys,

238   employing 934 measurements each, and the difference in resolution between the optimized and

239   standard survey. The resolution of the standard survey shows the usual distribution with high

240   resolution close to the electrodes, and a fast decline with increasing distance from the

241   electrodes. Within the target area a similar behaviour can be found; the upper part is perfectly

242   resolved, while the lower part exhibits a resolution < 0.3. The optimization is set to improve

243   the resolution within this target area. All tested values of β gain a higher resolution than the

244   standard survey in this part of the imaging plane, and image more than half of the target area

245   with a resolution > 0.9. While for $\beta = 0.0$, the entire imaging plane shows high resolution,

246   especially close to the surface, and increases with depth, for higher β values high resolution is

247   only achieved close to the target area. The higher β the fewer electrodes are used and the smaller

248   the well-resolved area becomes. The difference between optimized and standard resolution

249   highlights this behaviour (Figure 3 e-g). While for $\beta = 0.0$ the resolution in the target area

250   improves by more than 0.5, which is an increase of more than 100 %, considerable

251   improvements are also achieved in nearly the entire imaging plane, except in areas close to the

252   surface towards the boundaries, where the resolution is slightly smaller than for the standard

253   survey. In the target area, $\beta = 2.0$ provides comparable increases in resolution to $\beta = 0.0$,

254   improvements of up to 0.35 are gained using $\beta = 5.0$. Outside the target, the area with improved

255   resolution decreases with increasing β, and areas with worse resolution increase. The parts of

256   the imaging plane with decreased resolution are linked to the smaller set of electrodes used. In

257   general, increasing β results in improved resolution that is increasingly focussed on the target

258   area. This has to be considered for practical applications. If the location of the area of interest

259   is known with high confidence, large values of β can be used, while if the target location is

260   more uncertain then smaller values of β should be used.

Fig. 3

261   The impact of the step size on the performance of the optimization was also investigated; Figure

262   4 shows the performance for step sizes of 2%, 5%, and 10%. The main difference is when

263   additional electrodes are added to the survey during the optimization. Generally, step sizes of

264   5% and 10% tend to add more electrodes at a single iteration than added when using a step size

265   of 2%. This is particularly evident when the optimized set comprises about 5100 measurements.

266   At step sizes of 10% and 5%, ten and seven electrodes are added, respectively, while for 2%

267   only one additional electrode is used. Those differences in the use of electrodes also cause the

268   differences in relative resolution obtained by the different step sizes. The effect is comparably

269   small for optimized sets comprising less than 5500 measurements, but becomes more

270   significant for larger measurement sets, where differences in the relative resolution reach 0.11.

271   This larger difference is caused by a 2% step size using 13.8% fewer electrodes than employed

272   for a step size of 10%. Figure 4b shows that where the same number of electrodes are used,

273 regardless of step size, the optimized relative resolution is virtually identical. With the

274 increasing number of iterations, the calculation times increase considerably; while a 10 % step

275 size was calculated in 7.4 h, 5 % took 15.4 h, and 2% 26.3 h.

Fig. 4

276 The actual imaging performance of the survey designs is shown in Figure 5, where inverted

277 resistivity models are presented. In the forward model (Figure 5a), the area for which the

278 resolution was optimized was given a resistivity of 10 Ωm, while the background had a

279 resistivity of 100 Ωm. The forward problem was implemented and solved in Res3DMod

280 (Geotomo Software, Malaysia). The synthetic data were contaminated with voltage-dependent

281 noise defined as:

$$|e| = a + b|R_t|, \tag{7}$$

283 with $a = 0.05\ \Omega$, and $b = 0.02$.

284 All models were inverted using an L1 norm on the model roughness, and the data were fitted

285 to their respective errors ($\chi^2 = 1.0$). The comprehensive set, forming the benchmark for this

286 comparison, is able to delineate the target in its correct position and approximate extent; the

287 shape can be recognized in the inverted resistivity model, but is considerably smoothed and

288 imaged with a higher vertical extent. The target area is imaged with a minimum resistivity of

289 34.4 Ωm and a mean of 52.3 Ωm, while the background has a mean resistivity of 95.1 Ωm. The

290 standard survey, employing only 934 measurements (1.3% of the comprehensive set) and all

291 32 possible electrode location, fails in imaging the true shape and depth of the target. It is

292 imaged as a subvertical feature with a mean resistivity of 53.4 Ωm in the true target location,

293 thus 1.1 Ωm higher than imaged by the comprehensive survey. The background resistivity has

294 a mean of 96.8 Ωm. The optimized set images the target in a shape similar to the comprehensive

295 set and with a mean resistivity of 45.2 Ωm and a minimum of 24.1 Ωm, thus closer to the true

296 resistivity model than imaged by the standard survey. The background is imaged at a mean

297 resistivity of 80.7 Ωm, and thus lower than for the comprehensive and standard surveys. This

298 is an effect of the lower resolution outside the target area. The uncentered Pearson r correlation

299 coefficient of the target area showed a stronger correlation between the true resistivity model

300 and optimized inversion result ($r_{opt} = 0.89$) than between the true resistivity model and standard

301 survey results ($r_{standard} = 0.78$). Similarly, the root-mean-squared (RMS) difference between the

302 true resistivity model and the results of the optimized survey was 32.7 Ωm, while it was 43.7

303 Ωm for the standard survey. Outside the target area is where the optimized set performs worse

304 than the standard survey. Thus, within the target horizon the optimized set images the true

305 resistivity more accurately than the standard survey, despite employing 56% less electrodes,

306 but the smaller number of employed electrodes causes a loss of imaging performance outside

307 the target.

Fig. 5

308 Both the spatial distribution of possible electrode locations and the electrodes comprising the

309 initial set are variables affecting the results of the optimization. To show this, we recalculated

310 the optimization using $\beta = 5.0$ but employing a different initial set of electrodes, with four

311 electrodes being placed close to the model boundaries, and three close to the target (white dots

312 in Figure 6, initial set B). The results are similar to what was achieved with the first initial set

313 comprising electrode locations directly over the target (initial set A). The resolution within the

314 target is virtually identical (compare Figures 3d and 6a), but more resolution is retained in

315 shallow areas close to the model boundaries. The similarity between the two results is

316 highlighted when comparing the difference of the optimized resolution to the resolution of the

317 standard survey (Figures 3g and 6b). In both cases, the optimized survey shows increased

318 resolution in lower parts of the target area, which extend outside the target boundaries. Using

319 initial set B this area outside the target is smaller than for initial set A. The inverted resistivity

320 model shows the target with a similar shape to that imaged using the optimized survey of initial

321 set A, but with a shape more comparable to the results obtained by the comprehensive survey.

322   This is an effect of a higher fraction of measurements with low geometric factor in the

323   optimized survey of initial set B. These measurements have a smaller error and thus lead to a

324   better imaging performance. The additional use of measurements close to the model boundaries

325   cause a lower reduction of resolution in this area and improved the recovery of the true

326   resistivity in these parts of the model. Despite the different initial sets of electrodes, the

327   performance of the optimizations are comparable in both the achieved resolution of the target

328   and used electrode locations.

Fig. 6

329

4 3D MEASUREMENT GRID

331   Extending surveys into three dimensions usually leads to significant increases in the number

332   of electrode locations and measurements. Hence, this is where the proposed optimization

333   methodology is expected to show the greatest benefits. In order to test the optimization, a 3D

334   synthetic example was designed, comprising 117 electrodes, arranged in a grid of 13 electrodes

335   along the x-axis, and 9 electrodes along the y-axis. The setup replicates a typical embankment

336   situation, e.g. a flood embankment or mining tailings dam, where electrodes are deployed only

337   on one side (Figure 7). To resemble typical conditions, the "embankment" has a 1 in 2 slope

338   (Glendinning et al., 2014), miniaturized into an assumed laboratory tank set-up being 1 m long

339   and wide, with an embankment height of 0.25 m. The results of this synthetic study are used in

340   the following laboratory study, testing the methodology on real data. The electrode spacing in

341   x-direction was chosen to be 0.075 m, and 0.1 m in the y-direction. The impact of different

342   model mesh sizes on the performance of the optimization was tested and showed only

343   negligible effects. Thus, a relatively coarse discretization using 9711 tetrahedral elements was

344   used. The target was defined as a rectangular prism, with dimensions of 0.68 m, 0.3 m, and

345   0.06 m along the x, y, and z-directions. It was placed centrally at the base of the slope,

346   resembling an area that could potentially be affected by soil piping or a different failure type

347   at the base of an embankment. Neumann-boundary conditions were used at the outer and lower

348   model boundaries to account for the insulating tank walls. The comprehensive set comprised a

349   subset of alpha and beta configuration, including inline, crossline, and diagonal alpha and beta-

350   type configurations, as well as equatorial beta-type configurations (sensitivity patterns of these

351   measurement types are discussed in detail in Loke et al., 2014), with a maximum geometric

352   factor of $K_{max} = 345$ m (equal to a dipole-dipole geometric factor for $a = 1$ and $n = 10$) and a

353   geometric sensitivity of $s/K = 100$ m^{-1}. The grid of electrodes extended close to the model

354   boundaries, which were found to have a significant impact on the calculation of the geometric

355   factor. Thus, the comprehensive set was filtered on the geometric factors calculated using a

356   homogeneous forward model incorporating the correct boundary conditions (Loke et al., 2014);

357   after filtering it included 12755 measurements. The damping factor $\lambda = 0.05$ was chosen so

358   that the resolution at the base of the model was $R < 0.05$. The computation time of this

359   optimization was 10.2 h.

360   The initial set for the optimization comprised six electrodes, located centrally above the target

361   volume, and 20 measurements. Considering the optimization performance obtained on the

362   linear electrode array example, the 3D optimization was run using a step size of 10% and for a

363   weighting exponent of $\beta = 5.0$ (Figure 8). Optimization studies often assume a homogeneous

364   model resistivity for generality, and previous studies have shown that moderate deviations from

365   this assumptions have negligible effects on the results (e.g., Stummer et al., 2004; Wilkinson

366   et al., 2006). In this 3D example we envisage to image a very strong resistivity contrast, which

367   could have a potential impact on the optimization as potential fields are considerably disturbed.

368   Thus, rather than testing the optimization performance regarding β and the step size, the effects

369   of the underlying resistivity model are investigated. Hence, optimized survey designs were

370   calculated assuming a homogeneous resistivity model of 10 Ωm, and a resistivity model with

371   a resistive target (5000 Ωm) in a 10 Ωm background medium. As a real data application is

372   considered, measurement errors are incorporated into the optimization (Wilkinson et al., 2012)

373   and assumed to be a function of the transfer resistance R_t (eq. 7).

374   Figure 7 shows the resolution of the comprehensive set for both situations. While for the

375   homogeneous model (Figure 7a) the target is well resolved ($R > 0.5$) between $x = 0.4$ and $x =$

376   0.6 m, defining it as a resistive feature lowers the resolution within the target significantly (R

377   < 0.05). This is because current will flow predominantly through the background medium and

378   not through the highly resistive target volume.

Fig. 7

379   This considerable change in the comprehensive set resolution affects the performance of the

380   optimization (Figure 8), as different measurements will need to be chosen to resolve a resistive

381   target, compared to a target with a similar resistivity to the background medium. Generally, the

382   lower the resolution in the resistive target, the lower the relative resolution that is achieved at

383   a given number of measurements, compared to the optimization using a homogeneous

384   resistivity model; the largest difference $\Delta S = 0.31$ occurs with the optimized set comprising

385   3345 measurements. Although, the absolute improvement is smaller for the resistive target, the

386   general shape of the optimization curves are comparable. Also the number of employed

387   electrode locations is similar, with the optimization on the homogeneous resistivity model

388   usually employing 2-6 electrodes fewer than on the resistive target. A significant difference

389   can only be observed during the first 25 iterations (< 180 measurements), where the

390   optimization on the homogeneous model uses up to 25 electrodes fewer than for the resistive

391   target, where more electrodes are required to gain improvements.

Fig. 8

392   Figure 8 also shows the relative resolution of the standard survey design, comprising 1591

393   dipole-dipole and Wenner-Schlumberger configurations, both inline and crossline. As for the

394   comprehensive and optimized surveys, the relative resolution of the standard design on the

395   resistive target is significantly smaller ($S = 0.06$) than on the homogeneous model ($S = 0.21$).

396 For the same number of measurements the relative resolution achieved using optimized survey

397 designs is 0.54 and 0.26 for the homogeneous model and resistive target, respectively, increases

398 in resolution of 157 % and 333 %. Thus, the optimization survey design calculated on the

399 resistive target should provide better results, given that the underlying assumption of a strong

400 resistivity contrast holds true. Those considerable improvements are achieved using 28 and 26

401 electrodes fewer than used in the standard survey (homogeneous model and resistive target,

402 respectively), reductions of 24 % and 22 %.

403 Figure 9 shows the distribution of the resolution along a slice through the model domain at $y =$

404 0.5 m, both for the standard and optimized surveys. For the homogeneous model (compare

405 Figure 9c against 9a) resolution is improved particularly in deeper parts of the model, while,

406 e.g., at the top of the slope resolution decreases. Within the target volume, the largest absolute

407 increase in resolution can be found at the shallow parts between $x =$ 0.5 and 0.65 m. While

408 deeper parts show smaller absolute increases in resolution, the increase relative to the standard

409 survey exceed 100 % and are thus higher than for the shallow parts. Similarly to the results

410 obtained on the linear electrode array example, the large weighting exponent of $\beta =$ 5.0 forces

411 improvements more strongly towards the target volume, while resolution decreases away from

412 it. The reduction is strongest close to the boundaries of the model domain (Figure 9e), where

413 also fewer electrodes are employed. This observation is independent of type of resistivity

414 model used for the optimization, as similar patterns of resolution improvements and reductions

415 can be found for the optimization of the resistive target (Figure 9f). However, improvements

416 relative to the standard survey are considerably higher within the target volume (exceeding 200

417 %, comparing Figures 9b and d), despite the absolute values remaining low. This comparison

418 to the resolution of the standard survey shows that a precise knowledge of the target's locations

419 is not a prerequisite for improved imaging results, as the resolution increases in a wider area

420 around the target employing an optimized survey design.

421   Figures 9e and f also show the employed electrode locations. The pattern is comparable for the

422   two optimizations. Electrodes along the $x = 0.0$, and $y = 1.0$ boundaries tend to be rejected by

423   the optimization routine, as well as electrodes on top of the slope. This is somewhat surprising,

424   as for imaging a deeper target, conventional survey designs would usually employ larger

425   electrode spacing. However, measurements with large electrode spacing usually have larger

426   measurement errors and are therefore "penalized" in the optimization. This exercise shows that

427   those outer electrodes are not required to gain high resolution in the target volume, and

428   highlights the potential of this optimization approach to increase the efficiency of ERT

429   imaging, by reducing costs for cables and instrumentation.

430   The imaging capability of the different survey designs was tested by defining the target volume

431   as a resistive feature (5000 Ωm) within a 10 Ωm background material. This may represent, e.g.,

432   a clay embankment with a structural defect at its base, which could cause soil piping or slope

433   instabilities, and is of the same order of magnitude as expected for the laboratory experiments.

434   All synthetic data were contaminated with 2% voltage-dependent noise, and the inversion

435   converged to fit these data within its error levels, using the same inversion parameters as for

436   the linear electrode array example.

437   The results of the comprehensive set (Figure 10a) resemble the distribution of the resolution

438   (Figure 7); the target is imaged with a strong resistivity contrast between $x = 0.4$ m and 0.8 m,

439   showing resistivities above 30 Ωm, with a maximum of 163.5 Ωm. The mean resistivity in the

440   target volume is 33.0 Ωm. This shows the effect of the lower resolution within a resistive target;

441   the difference between the imaged and the true resistivity (5000 Ωm) is more than one order of

442   magnitude. Its centre is imaged with the highest contrasts, which decrease towards the edges,

443   imaging it with an oval shape. With increasing distance along the x-direction, and thus

444   increasing depth from the surface, the target becomes less well resolved, with smaller resistivity

445   contrasts and a shift of the highest values to shallower layers. Thus, the resistive target seems

446   to have an apparent dip. Between $x = 0.8$ and 1.0 m, the resistivity contrast becomes smaller,

447   and therefore could be overprinted by natural resistivity variations in real applications. Fig. 10

448   The standard survey, using about 12.5 % of the measurements of the comprehensive set, images

449   the target with a smaller resistivity contrast than the comprehensive set, having a maximum of

450   67.6 Ωm and a mean resistivity in the target volume of 22.4 Ωm. Considering an iso-volume

451   at 30 Ωm, the target is imaged extending from $x = 0.41$ to 0.71 m, while for the comprehensive

452   set, it extend from 0.41 to 0.80 m. Deeper parts of the model, $x > 0.70$ m, show lower

453   resistivities than imaged with the comprehensive set and the contrast is less sharply defined.

454   The optimized survey designs image the target with a higher resistivity contrast and larger

455   extent than the standard survey, independently of their underlying resistivity model. However,

456   the target is imaged with a higher maximum resistivity ($\rho_{max} = 113.8$ Ωm) and mean resistivity

457   in the target volume ($\rho_{mean} = 28.1$ Ωm) when using the resistive target in the optimization, than

458   if using a homogeneous model ($\rho_{max} = 100.5$ Ωm, $\rho_{mean} = 26.2$ Ωm). Considering again a 30

459   Ωm iso-volume, the target is imaged to extend from 0.40 to 0.73 m for both optimized surveys.

460   The improved performance of the optimized surveys is highlighted when looking at the

461   uncentered Pearson correlation coefficient. While for the standard survey a Pearson correlation

462   coefficient of $r_{standard} = 0.29$ is obtained, for the optimized set the correlation is better with r_{hom}

463      $= 0.31$ and $r_{resistive} = 0.33$. Thus, in comparison to standard survey designs improved imaging

464   results can be obtained using the optimization methodology, despite requiring up to 24 % fewer

465   electrodes. Even higher reductions in number of electrodes used can be expected for smaller

466   targets.

467

468   **5 LABORATORY EXPERIMENT**

469   To test the applicability of the optimization methodology to measured data, a laboratory tank

470   was prepared as described in the previous synthetic example. To ensure a mostly homogeneous

471   background medium, a 1 m × 1 m laboratory tank was filled with pre-prepared, moist

472   (volumetric moisture content (VMC) of 0.31 m^3/m^3) pottery clay of low shrinkage (< 5 %), and

473   a mean resistivity of 17 Ωm. The target was constructed using kiln-dried silica sand with a

474   grain size below 0.5 mm and a VMC < 0.04 m^3/m^3; its resistivity was estimated to be > 5000

475   Ωm. Electrode layout and surface topography was as described for the synthetic example. Data

476   were acquired using a Geolog2000 GeoTom system (employing one channel at 8 1/3 Hz) and

477   were measured in normal and reciprocal configurations, where the reciprocal measurement is

478   equivalent to the normal, but with interchanged current and injection dipoles (LaBrecque et al.,

479   1996). The data were defined as the mean of the two measurement, and the error as the standard

480   error in the mean, which is referred to as reciprocal error hereafter. The measurement sequence

481   was reordered to minimize potential polarization effects of the electrodes (Wilkinson et al.,

482   2012). Despite using small electrodes (1.55 mm diameter, 5 mm length) contact resistances

483   between electrodes and clay were below 1.1 kΩ. The data quality was very good, with about

484   99 % of the data having reciprocal errors below 5%. Analysis of the reciprocal error distribution

485   (Koestel et al., 2008) confirmed the applicability of the previously introduced linear error

486   model (equation 7), but measurement errors were actually lower, so coefficients of $a = 0.0025$

487   Ω and $b = 0.003$ were used to weight the data in the inversion. The data were inverted using

488   E4D (Johnson et al., 2010), employing the same inversion parameters as for synthetic

489   examples. The inversions converged fitting the data to their corresponding error levels, at RMS

490   misfits between modelled and measured data of 2.1 – 3.2 %.

491   The results are similar to those obtained in the synthetic model, but with the target showing a

492   considerably higher resistivity (Figure 11). Thus, the true target resistivity likely to be higher

493   than was assumed in the synthetic model and used for the calculation of the optimized survey

494   design. This would reflect field usage of this technique where the actual resistivity of the target

495   area is unlikely to be known exactly. The comprehensive survey images the target with a

496   maximum resistivity of 969.7 Ωm and a mean resistivity in the target volume of 108.5 Ωm.

497   The resistive anomaly follows mostly the actual target location, with a slight overestimation in

498   depth for shallow parts (0.4 m $< x <$ 0.7 m) and an underestimation in deeper parts ($x >$ 0.8 m).

499   Thus, the target shows an apparent dip as in the previous section. The 60 Ωm iso-volume

500   highlights this dip, but images the target with a reasonable accuracy (Figure 11a). The standard

501   survey shows the shallow parts of the target at the correct location, but with a smaller resistivity

502   contrast; the maximum resistivity is 264.6 and the mean target resistivity 49.9 Ωm. The

503   apparent dip is more pronounced, as the resistive anomaly bends towards shallower depths and

504   resistivities decrease considerably. The 60 Ωm iso-volume extends only until $x =$ 0.84 m, and

505   becomes narrow for $x >$ 0.7 m (Figure 11b). The results for the optimized survey assuming a

506   homogeneous resistivity model show some improvement compared to the standard survey; the

507   target is imaged with a maximum resistivity of 404.0 Ωm and a mean resistivity of 62.6 Ωm.

508   The narrowing of the 60 Ωm iso-volume for $x >$ 0.7 m is less pronounced, but extends only to

509    $x =$ 0.81 m. Better imaging results are achieved using the optimization assuming a resistive

510   target, where the target volume is imaged with a maximum of 490.7 Ωm and a mean of 68.2

511   Ωm. The 60 Ωm iso-volume is comparable to the one obtained from the comprehensive set.

512   Thus, the resistivity values obtained from the optimized surveys are closer to the

513   comprehensive set than imaged using the standard survey design.   Fig. 11

514   Even though the resistivity distribution in the tank can be estimated, variations in degree of

515   compaction of the material and moisture content may cause variations. Therefore, the

516   resistivity model of the comprehensive survey is taken as the imaging benchmark. Considering

517   the uncentered Pearson correlation and the RMS difference highlights the improved

518   performance of the optimized survey designs compared to the standard design. The Pearson

519   correlation coefficient between the imaged resistivities using the comprehensive and standard

520   survey design is $r_{standard} =$ 0.88, while for optimization assuming a homogeneous model and a

521   resistive target it is $r_{hom} = 0.94$ and $r_{resistive} = 0.96$, respectively. This highlights that if very large

522   resistivity contrasts exist in the subsurface, these should be accounted for in the optimization,

523   as it has a significant effect on the model resolution, as shown in Figures 6 and 8. The RMS

524   differences between the imaged resistivities obtained from the optimized sets and the

525   comprehensive set are $RMS_{hom} = 32.7$ % and $RMS_{resistive} = 29.8$ %, while it is $RMS_{standard} =$

526   40.4 % for the standard survey design. This highlights the considerable improvements that can

527   be achieved when using the proposed optimization methodology, while reducing the amount

528   of required electrode locations.

529   **6 DISCUSSION AND CONCLUSION**

530   Optimization of survey design can usually by categorised as (1) trying to find optimum

531   measurement configurations on a given set of electrode locations, or (2) selecting electrode

532   locations based on their comprehensive resolution. This paper presents a modification to the

533   "Compare-R" algorithm, which combines the two approaches by introducing an additional

534   weight penalizing the addition of electrode locations to the optimized set.

535   Tests on synthetic examples showed that optimization step size and model discretization have

536   negligible effects on the results. Experimenting with different weighting exponents β, which

537   controls how much the addition of electrodes to the optimized set is penalized, showed that

538   higher values of β cause more focussed improvements in resolution and the use of smaller

539   numbers of electrodes, with the drawback of decreasing resolution away from the target

540   volume. Therefore, high values of β should be used if the target location and size is well known,

541   and smaller values if it is more uncertain. For an example using a linear electrode array, it was

542   shown that superior resolution compared to a standard survey design can be achieved, despite

543   using 56 % fewer electrodes. To test the impact of the number of electrodes in the

544   comprehensive set, the optimization was run for 16 and 64 electrodes, half and twice the

545 number of electrodes in the shown example. While for 16 electrodes, all electrodes are required

546 to achieve high resolution in the target area, using double the amount of electrodes had no

547 considerable impact on the outcome of the optimization, as electrodes were chosen in the same

548 area as shown for a comprehensive set of 32 electrodes.

549 An investigation of the effect of the mesh discretisation on the calculated sensitivities showed

550 that unstructured tetrahedral meshes can introduce a slight degree of asymmetry into the results.

551 This is caused by the tetrahedral elements not having the same symmetry as the distribution of

552 electrodes and can be overcome by using a mesh discretization with different polyhedra, such

553 as cuboids.

554 The methodology was also tested on a 3D synthetic example and verified with a laboratory

555 experiment. The 3D example imaged a structural, highly resistive, defect within a miniaturized

556 embankment model. Here the effect of the underlying resistivity model on the performance of

557 the optimization was tested. By accounting for the resistive target better results were obtained,

558 increasing the uncentered Pearson correlation coefficient between the imaged resistivities and

559 the forward model from $r_{standard} = 0.29$ for the standard survey to $r_{resistive} = 0.33$ for the optimized

560 survey assuming a resistive target. The uncentered Pearson correlation between model and

561 imaged resistivities was $r_{hom} = 0.31$ for the optimized survey assuming a homogeneous

562 medium. This is in agreement with previous studies, which showed that small variations in the

563 resistivity distribution have negligible effects on the optimization (e.g., Athanasiou et al.,

564 2006). Here, accounting for a strong resistivity contrast improved the performance of the

565 optimization, but not significantly. Although no marked improvement was obtained, both

566 optimized surveys were able to image the resistive target better than the standard survey design

567 while using fewer electrodes. This was true for the synthetic models and the laboratory

568 experiment. In the latter, accounting for the resistive target helped to increase the Pearson

569 correlation coefficient between optimized and the comprehensive sets from $r_{hom} = 0.94$ to

570   $r_{resistive} = 0.96$, which were both superior to the Pearson correlation of the standard survey

571   design ($r_{standard} = 0.88$). Here a high weighting factor of $\beta = 5.0$ was used, thereby achieving

572   this improved resolution despite using up to 24 % fewer electrodes than a comparable standard

573   survey. Note that using smaller values of β would yield higher resolution within the target area,

574   with the cost of using more electrodes. Higher values were tested but reduced the number of

575   electrodes only marginally while causing a further decrease in resolution of the target.

576   This study shows that by using optimization algorithms that can penalize the number of

577   electrodes used, the efficiency of resistivity imaging and monitoring can be increased by

578   reducing its costs. It may offer the opportunity for high-resolution resistivity imaging using

579   smaller numbers of electrodes and therefore cables, but also using measurement systems

580   capable of addressing only a limited number of electrodes. This may be particularly important

581   for complex monitoring studies with limited accessibility, or where the installation of

582   electrodes may be difficult or detrimental to the structural integrity. For this purpose, values of

583   $\beta > 5$ may be chosen to reduce the number of electrodes to a minimum. On the other hand, if

584   measurement time is a priority, smaller values of β may be used, allowing to gain high

585   resolution at comparably small measurement sets. We envisage the greatest benefit of the

586   presented approach would be for monitoring or characterisation studies where information

587   about the location of areas of interest are available prior to the survey, e.g., for leaking flood

588   embankments, landslides with well-defined slip surfaces, or contamination studies with

589   reasonably well known hydrology. Additional research is required to implement further

590   constraints on the survey design, such as *a priori* limitations regarding the maximum number

591   of electrode locations, or pre-defined maximum lengths of survey lines, but also to investigate

592   the practical performance of recently developed measurement configurations (Falco et al.,

593   2013; Szalai et al., 2015, 2014, 2002). Recent research of Loke et al. (2015) shows that

594   calculation times for the optimization can be reduced by assuming symmetry of the

595 measurement configurations and exploiting developments in the GPU technology. Comparing

596 their calculation times to the calculation times presented here, GPU and other computational

597 developments may reduce the calculation time of the presented approach by up to 100 times.

598 Smaller calculation times will certainly increase the applicability of the survey optimization

599 and may help to investigate larger-scale problems.

600

601 **ACKNOWLEDGMENTS**

REFERENCES

Alfouzan, F.A., Loke, M.H., Nawawi, M.N.M., 2010. An evaluation of optimization strategies to automatically select the optimal set of array configurations for 2D electrical imaging surveys. J. Geophys. Eng. 7, 332–342. doi:10.1088/1742-2132/7/3/011

Athanasiou, E., Tsourlos, P., B. Papazachos, C., N. Tsokas, G., 2006. Optimizing Resistivity Array Configurations by Using a Non-Homogeneous Background Model, in: Near Surface 2006. Helsinki, pp. 4–6. doi:10.3997/2214-4609.201402687

Athanasiou, E.N., Tsourlos, P.I., Papazachos, C.B., Tsokas, G.N., 2009. Optimizing Electrical Resistivity Array Configurations by Using a Method Based on the Sensitivity Matrix, in: Near Surface 2009. Dublin, pp. 7–9. doi:10.3997/2214-4609.20147025

Benisch, K., Köhn, D., al Hagrey, S., Rabbel, W., Bauer, S., 2015. A combined seismic and geoelectrical monitoring approach for CO2 storage using a synthetic field site. Environ. Earth Sci. 73, 3077–3094. doi:10.1007/s12665-014-3603-0

Curtis, A., 1999. Optimal design of focused experiments and surveys. Geophys. J. Int. 139, 205–215. doi:10.1046/j.1365-246X.1999.00947.x

Curtis, A., Maurer, H., 2000. Optimizing the design of geophysical experiments: Is it worthwhile? Lead. Edge 19, 1058–1062. doi:10.1190/1.1438475

Daily, W., Ramirez, A., Binley, A., 2004. Remote Monitoring of Leaks in Storage Tanks using Electrical Resistance Tomography: Application at the Hanford Site. J. Environ. Eng. Geophys. 9, 11–24. doi:10.4133/JEEG9.1.11

Dumont, G., 2017. Geophysical characterization and monitoring of a municipal solid waste landfill. Université de Liège. doi:http://hdl.handle.net/2268/206929

Falco, P., Negro, F., Szalai, S., Milnes, E., 2013. Fracture characterisation using geoelectric null-arrays. J. Appl. Geophys. 93, 33–42. doi:10.1016/j.jappgeo.2013.03.005

Furman, A., Ferré, T.P., Heath, G.L., 2007. Spatial focusing of electrical resistivity surveys considering geologic and hydrologic layering. GEOPHYSICS 72, F65–F73. doi:10.1190/1.2433737

Gance, J., Malet, J.-P., Supper, R., Sailhac, P., Ottowitz, D., Jochum, B., 2016. Permanent electrical resistivity measurements for monitoring water circulation in clayey landslides. J. Appl. Geophys. 126, 98–115. doi:10.1016/j.jappgeo.2016.01.011

Glendinning, S., Hughes, P., Helm, P., Chambers, J., Mendes, J., Gunn, D., Wilkinson, P., Uhlemann, S., 2014. Construction, management and maintenance of embankments used for road and rail infrastructure: implications of weather induced pore water pressures. Acta Geotech. 9, 799–816. doi:10.1007/s11440-014-0324-1

Godio, A., Arato, A., Chiampo, F., Ruggeri, B., Di Addario, M., Fischetti, M., Perissinotto, E., 2015. Liquid injection to enhance biogas production in landfills for pretreated municipal solid wastes - BIO.LEA.R. Project (life+program). Environ. Eng. Manag. J. 14, 1623–1636.

Grellier, S., Guerin, R., Robain, H., Bobachev, A., Vermeersch, F., Tabbagh, A., 2008. Monitoring of Leachate Recirculation in a Bioreactor Landfill by 2-D Electrical Resistivity Imaging. J. Environ. Eng. Geophys. 13, 351–359. doi:10.2113/JEEG13.4.351

648   Hilbich, C., Hauck, C., Hoelzle, M., Scherler, M., Schudel, L., Völksch, I., Vonder Mühll, D.,
649   Mäusbacher, R., 2008. Monitoring mountain permafrost evolution using electrical
650   resistivity tomography: A 7-year study of seasonal, annual, and long-term variations at
651   Schilthorn, Swiss Alps. J. Geophys. Res. 113, F01S90. doi:10.1029/2007JF000799

652   Johnson, T.C., 2016. Real-time 4D electrical resistivity imaging of tracer transport within an
653   energically stimulated fracture zone, in: AGU Fall Meeting. San Francisco, USA.

654   Johnson, T.C., Slater, L.D., Ntarlagiannis, D., Day-Lewis, F.D., Elwaseif, M., 2012.
655   Monitoring groundwater-surface water interaction using time-series and time-frequency
656   analysis of transient three-dimensional electrical resistivity changes. Water Resour. Res.
657   48, 1–13. doi:10.1029/2012WR011893

658   Johnson, T.C., Versteeg, R.J., Ward, A., Day-Lewis, F.D., Revil, A., 2010. Improved
659   hydrogeophysical characterization and monitoring through parallel modeling and
660   inversion of time-domain resistivity and induced-polarization data. Geophysics 75,
661   WA27. doi:10.1190/1.3475513

662   Koestel, J., Kemna, A., Javaux, M., Binley, A., Vereecken, H., 2008. Quantitative imaging of
663   solute transport in an unsaturated and undisturbed soil monolith with 3-D ERT and
664   TDR. Water Resour. Res. 44, n/a-n/a. doi:10.1029/2007WR006755

665   Krautblatter, M., Verleysdonk, S., Flores-Orozco, A., Kemna, A., 2010. Temperature-
666   calibrated imaging of seasonal changes in permafrost rock walls by quantitative
667   electrical resistivity tomography (Zugspitze, German/Austrian Alps). J. Geophys. Res.
668   115, 1–15.

669   Kuras, O., Wilkinson, P.B., Meldrum, P.I., Oxby, L.S., Uhlemann, S., Chambers, J.E.,
670   Binley, A., Graham, J., Smith, N.T., Atherton, N., 2016. Geoelectrical monitoring of
671   simulated subsurface leakage to support high-hazard nuclear decommissioning at the
672   Sellafield Site, UK. Sci. Total Environ. 566–567, 350–359.
673   doi:10.1016/j.scitotenv.2016.04.212

674   LaBrecque, D.J., Miletto, M., Daily, W., Ramirez, A., Owen, E., 1996. The effects of noise
675   on Occam's inversion of resistivity tomography data. Geophysics 61, 538–548.

676   Loke, M.H., Chambers, J.E., Rucker, D.F., Kuras, O., Wilkinson, P.B., 2013. Recent
677   developments in the direct-current geoelectrical imaging method. J. Appl. Geophys. 95,
678   135–156. doi:10.1016/j.jappgeo.2013.02.017

679   Loke, M.H., Wilkinson, P.B., Chambers, J.E., 2010. Fast computation of optimized electrode
680   arrays for 2D resistivity surveys. Comput. Geosci. 36, 1414–1426.
681   doi:10.1016/j.cageo.2010.03.016

682   Loke, M.H., Wilkinson, P.B., Chambers, J.E., Uhlemann, S.S., Sorensen, J.P.R., 2015a.
683   Optimized arrays for 2-D resistivity survey lines with a large number of electrodes. J.
684   Appl. Geophys. 112, 136–146. doi:10.1016/j.jappgeo.2014.11.011

685   Loke, M.H., Wilkinson, P.B., Tejero-Andrade, A., Kruse, S., 2015b. Optimized Arrays for
686   Resistivity Measurements Confined to the Perimeter of a Survey Area, in: Near Surface
687   Geoscience 2015 - 21st European Meeting of Environmental and Engineering
688   Geophysics. Turin, pp. 6–10. doi:10.3997/2214-4609.201413793

689   Loke, M.H., Wilkinson, P.B., Uhlemann, S.S., Chambers, J.E., Oxby, L.S., 2014.
690   Computation of optimized arrays for 3-D electrical imaging surveys. Geophys. J. Int.

199, 1751–1764. doi:10.1093/gji/ggu357

Maurer, H., Friedel, S., 2006. Outer-space sensitivities in geoelectrical tomography. Geophysics 71, G93. doi:10.1190/1.2194891

Parsekian, A.D., Singha, K., Minsley, B.J., Holbrook, W.S., Slater, L., 2015. Multiscale geophysical imaging of the critical zone. Rev. Geophys. 53, 1–26. doi:10.1002/2014RG000465

Roux, E., Garcia, X., 2014. Optimizing an experimental design for a CSEM experiment: methodology and synthetic tests. Geophys. J. Int. 197, 135–148. doi:10.1093/gji/ggt525

Rucker, D., 2014. Investigating motion blur and temporal aliasing from time-lapse electrical resistivity. J. Appl. Geophys. 111, 1–13. doi:10.1016/j.jappgeo.2014.09.010

Schmidt-Hattenberger, C., Bergmann, P., Labitzke, T., Wagner, F., Rippe, D., 2016. Permanent crosshole electrical resistivity tomography (ERT) as an established method for the long-term CO_2 monitoring at the Ketzin pilot site. Int. J. Greenh. Gas Control 52, 432–448. doi:10.1016/j.ijggc.2016.07.024

Singha, K., Day-Lewis, F.D., Johnson, T., Slater, L.D., 2014. Advances in interpretation of subsurface processes with time-lapse electrical imaging. Hydrol. Process. 29, n/a-n/a. doi:10.1002/hyp.10280

Stummer, P., Maurer, H., Green, A.G., 2004. Experimental design: Electrical resistivity data sets that provide optimum subsurface information. GEOPHYSICS 69, 120–139. doi:10.1190/1.1649381

Supper, R., Ottowitz, D., Jochum, B., Kim, J., Römer, A., Baron, I., Pfeiler, S., Lovisolo, M., Gruber, S., Vecchiotti, F., 2014. Geoelectrical monitoring: an innovative method to supplement landslide surveillance and early warning. Near Surf. Geophys. 12, 133–150. doi:10.3997/1873-0604.2013060

Szalai, S., Lemperger, I., Metwaly, M., Kis, Á., Wesztergom, V., Szokoli, K., Novák, A., 2014. Multiplication of the depth of detectability using γ11n arrays. J. Appl. Geophys. 107, 195–206. doi:10.1016/j.jappgeo.2014.06.003

Szalai, S., Szarka, L., 2011. Expanding the possibilities of two-dimensional multielectrode systems, with consideration to earlier geoelectric arrays. J. Appl. Geophys. 75, 1–8. doi:10.1016/j.jappgeo.2011.06.020

Szalai, S., Szarka, L., Prácser, E., Bosch, F., Müller, I., Turberg, P., 2002. Geoelectric mapping of near surface karstic fractures by using null arrays. GEOPHYSICS 67, 1769–1778. doi:10.1190/1.1527077

Szalai, S., Wesztergom, V., Szokoli, K., Frigy, A., Prascer, E., 2015. Field Applicability of the g11n Configuration. 8th Congr. Balk. Geophys. Soc. doi:10.3997/2214-4609.201414151

Tsakirrbaloglou, K., Tsourlos, P., Vargemezis, G., Tsokas, G., 2016. An Algorithm for the Adaptive Optimization of ERT Measurements, in: Near Surface Geoscience 2016-22ond European Meeting of Environmental and Engineering Geophysics. p. 4. doi:10.3997/2214-4609.201601997

Tsourlos, P., Jochum, B., Supper, R., Ottowitz, D., Kim, J.H., 2016. Optimizing Geoelectrical Arrays for Special Geoelectrical Monitoring Instruments, in: Near Surface Geoscience

733 2016- 22ond European Meeting of Environmental and Engineering Geophysics. p. 4.
734 doi:10.3997/2214-4609.201601946

735 Uhlemann, S., Chambers, J., Wilkinson, P., Maurer, H., Merritt, A., Meldrum, P., Kuras, O.,
736 Gunn, D., Smith, A., Dijkstra, T., 2017. Four-dimensional imaging of moisture
737 dynamics during landslide reactivation. J. Geophys. Res. Earth Surf. 122, 398–418.
738 doi:10.1002/2016JF003983

739 Wagner, F.M., Günther, T., Schmidt-Hattenberger, C., Maurer, H., 2015. Constructive
740 optimization of electrode locations for target-focused resistivity monitoring.
741 GEOPHYSICS 80, E29–E40. doi:10.1190/geo2014-0214.1

742 Wang, Q., Zhang, X., Zhang, Y., Yi, Q., 2013. AUGEM: Automatically Generate High
743 Performance Dense Linear Algebra Kernels on x86 CPUs, in: Proceedings of the
744 International Conference for High Performance Computing, Networking, Storage and
745 Analysis on - SC '13. ACM Press, New York, New York, USA, pp. 1–12.
746 doi:10.1145/2503210.2503219

747 Wilkinson, P.B., Chambers, J.E., Lelliott, M., Wealthall, G.P., Ogilvy, R.D., 2008. Extreme
748 sensitivity of crosshole electrical resistivity tomography measurements to geometric
749 errors. Geophys. J. Int. 173, 49–62. doi:10.1111/j.1365-246X.2008.03725.x

750 Wilkinson, P.B., Loke, M.H.., Meldrum, P.I., Chambers, J.E., Kuras, O., Gunn, D.A., Ogilvy,
751 R.D., 2012. Practical aspects of applied optimized survey design for electrical resistivity
752 tomography. Geophys. J. Int. 189, 428–440. doi:10.1111/j.1365-246X.2012.05372.x

753 Wilkinson, P.B., Meldrum, P.I., Chambers, J.E., Kuras, O., Ogilvy, R.D., 2006. Improved
754 strategies for the automatic selection of optimized sets of electrical resistivity
755 tomography measurement configurations. Geophys. J. Int. 167, 1119–1126.
756 doi:10.1111/j.1365-246X.2006.03196.x

757 Wilkinson, P.B., Uhlemann, S., Meldrum, P.I., Chambers, J.E., Carrière, S., Oxby, L.S.,
758 Loke, M.H., 2015. Adaptive time-lapse optimized survey design for electrical resistivity
759 tomography monitoring. Geophys. J. Int. 203, 755–766. doi:10.1093/gji/ggv329

760

761
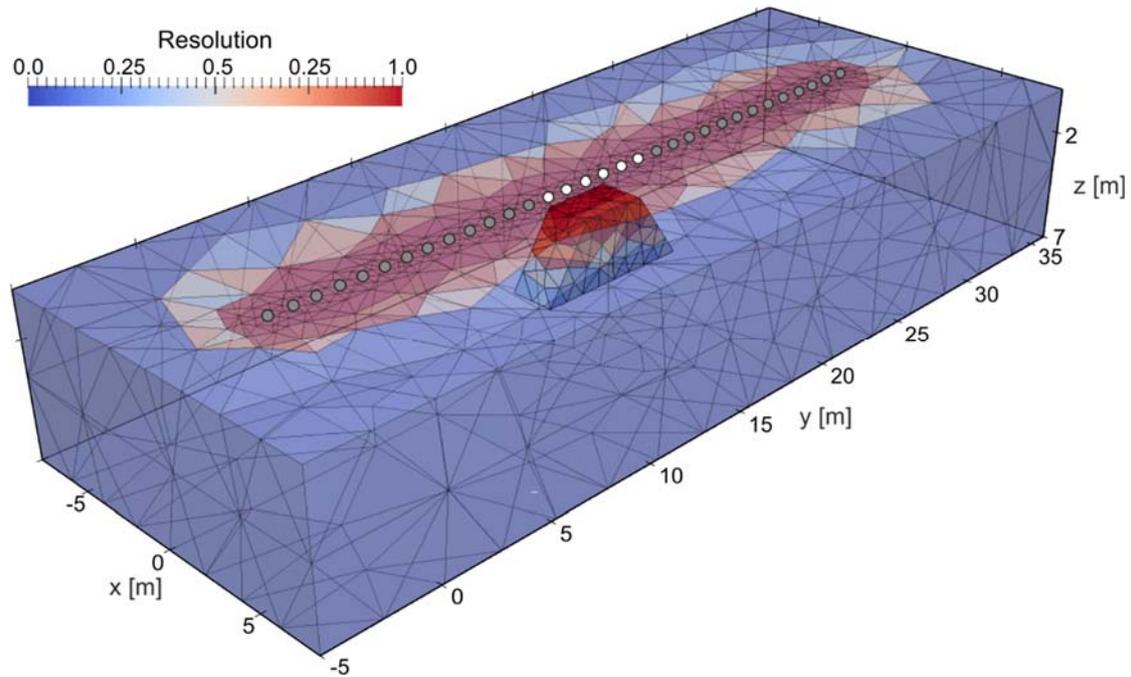
762 Figure 1 Comprehensive set model resolution (comprising 70555 measurements); grey lines represent
763 the model discretization. The target volume is shown opaque. Grey dots indicate possible electrode
764 locations; white dots indicate the initial set of electrodes. Note that the slight asymmetry is caused by
765 the discretization of the model.

766
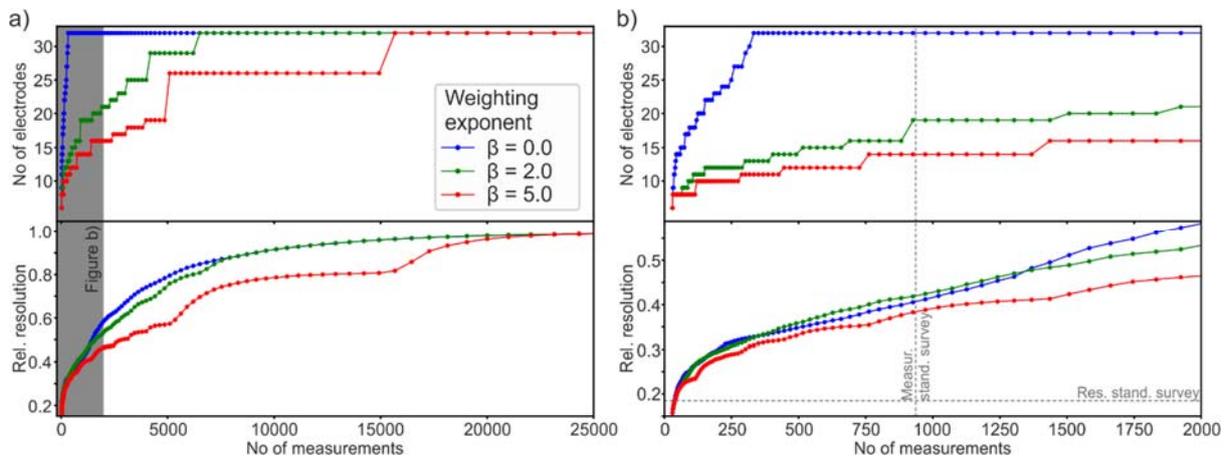
767

768 Figure 2 a) Optimization performance in terms of the relative resolution S and number of used
769 electrodes for weighting exponents β = 0.0, 2.0, and 5.0, employing a step size of 5%. The grey area
770 shows the range shown in b). b) subset of a) showing the results for the first 2000 measurements with
771 dashed lines indicating the number of measurements and relative resolution of a standard survey.

772

773
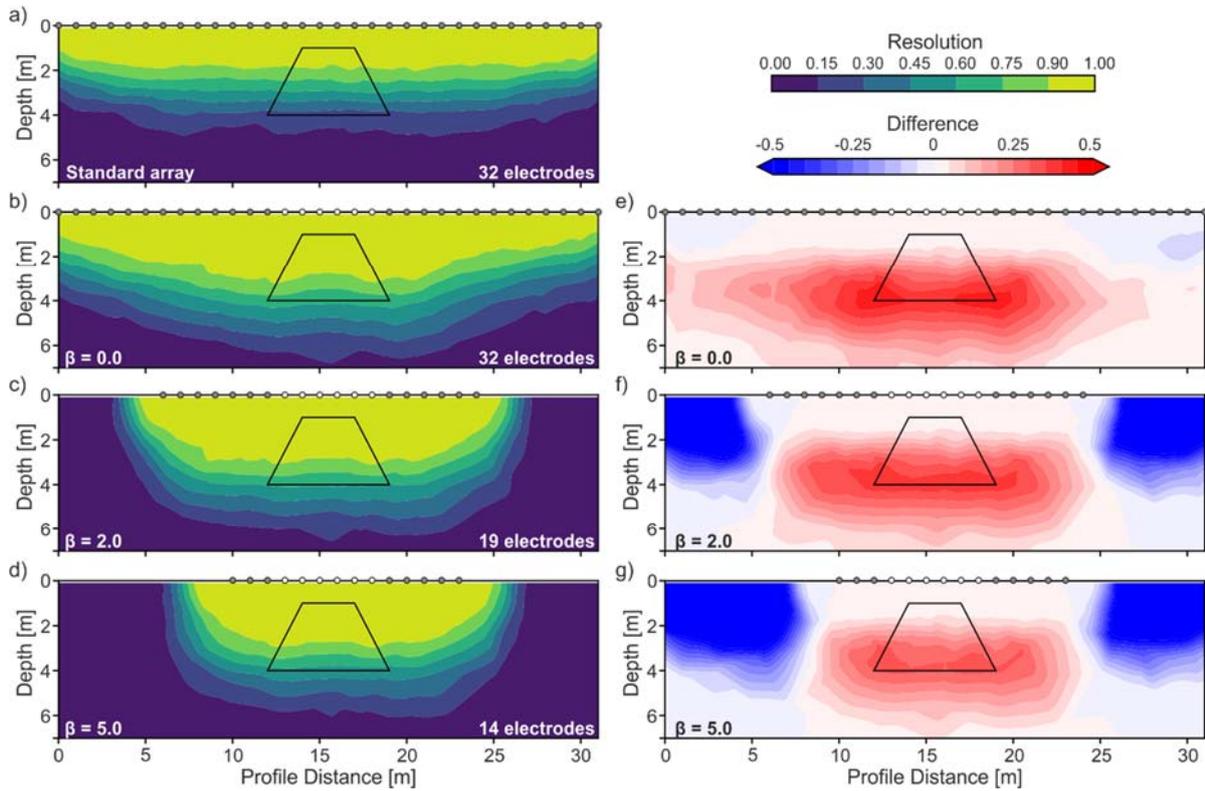
Figure 3 Model resolution for a) standard survey and b)-d) optimized surveys using β = 0.0, 2.0, and
5.0. e)-g) difference in model resolution between optimized and standard survey design. In all cases,
the resolution within the target volume increased compared to the standard survey. Dots indicate used
electrode locations; white dots show the initial set.

778

779
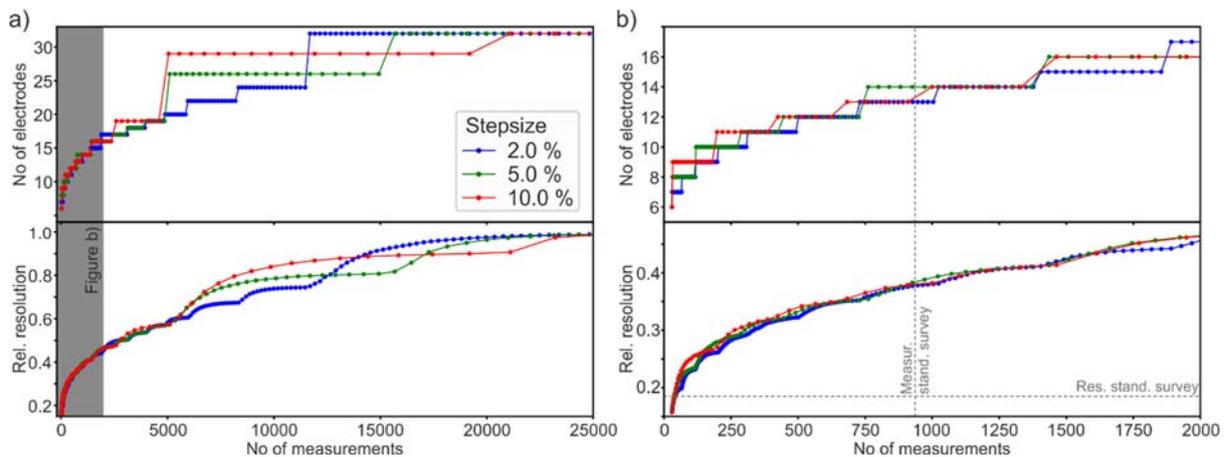
Figure 4 a) Optimization performance in terms of the relative resolution S and number of used
electrodes for β = 5.0 and different step sizes of 2%, 5%, and 10%. b) subset of a) showing the results
for the first 2000 measurements with dashed lines indicating the number of measurements and relative
resolution of a standard survey.

784

785
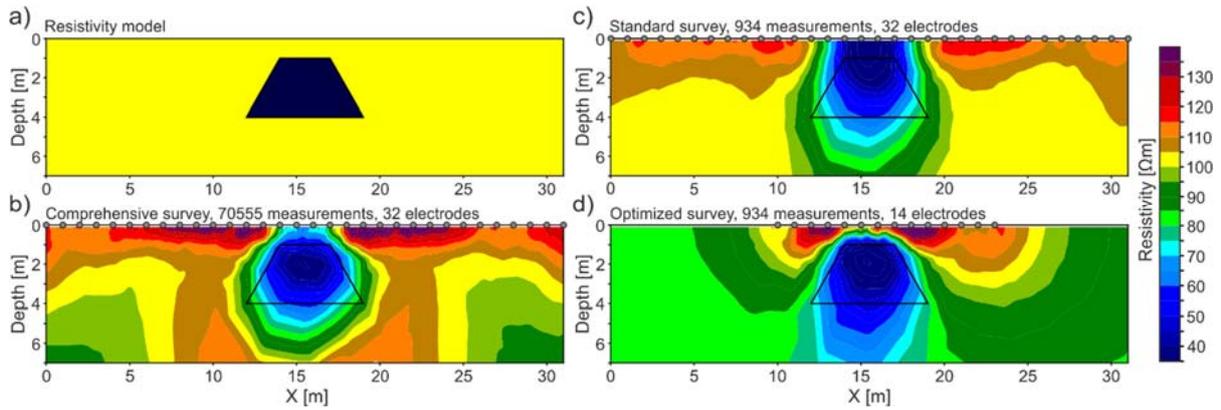
Figure 5 Resistivity models. a) resistivity model employed in the calculation of the synthetic data; b) inverted resistivity model using a comprehensive set of measurements, employing 70 555 measurements and 32 electrodes; c) inverted resistivity model using a standard survey design comprising 934 measurements and 32 electrodes; d) inverted resistivity model using an optimized survey comprising 934 measurements, but only 14 electrodes. Note that some asymmetry maybe introduced by the model discretization.

792

793
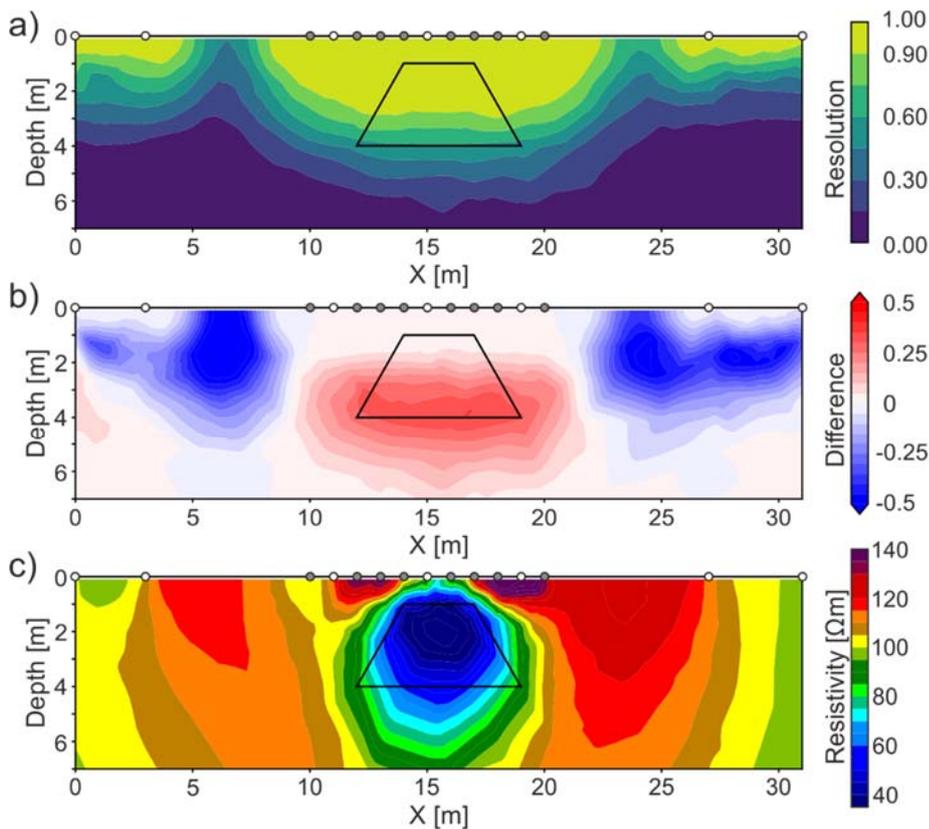
Figure 6 Results for an optimization using an initial set comprising four electrodes close to the section boundaries and three electrode close to the target. Electrode locations are shown as dots, with white dots indicating the initial locations. a) Resolution of the optimized survey, b) difference in resolution between optimized and standard survey, and c) inverted resistivity model as shown in Figure 5.

798

799
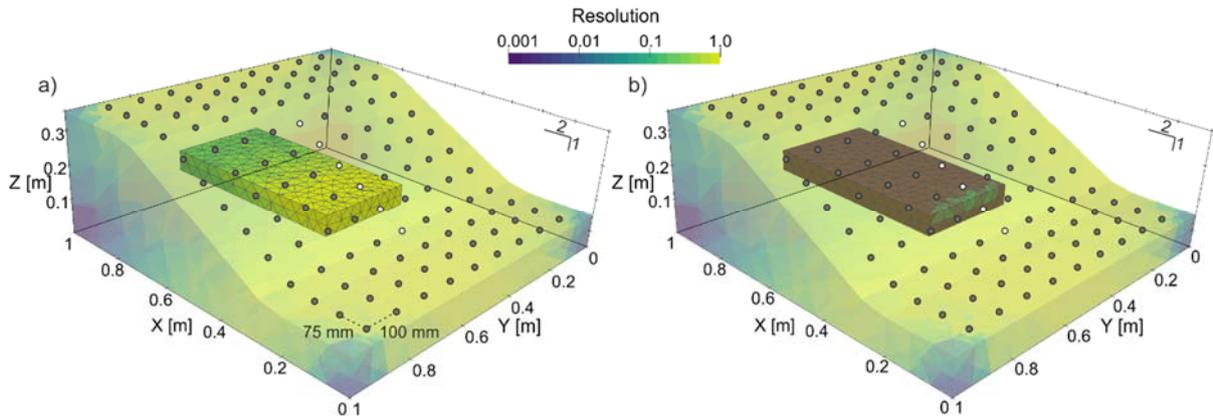
Figure 7 Resolution of the comprehensive set for the synthetic 3D example assuming a homogeneous resistivity distribution of 10 Ωm (a), and the target as having a resistivity of 5000 Ωm within a 10 Ωm background medium (b). The target volume is shown opaque. The dots show the electrode locations, with white dots indicating the initial set of six electrodes.

804

805
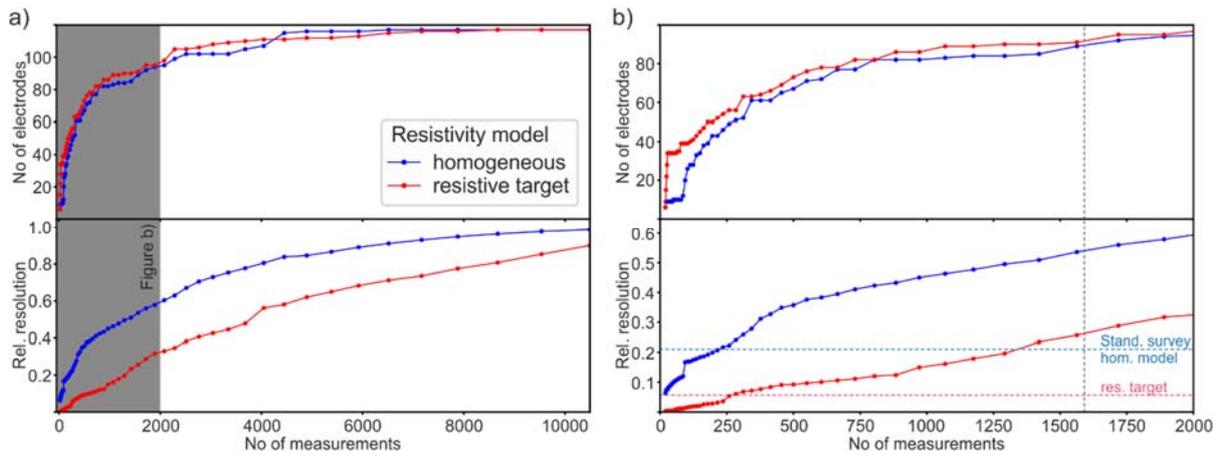
Figure 8 Optimization performance of the 3D example in terms of the relative resolution S and number of used electrodes for a weighting exponents β = 5.0, employing a step size of 10%, and two different resistivity models. The blue lines show the performance for a homogeneous resistivity model of 10 Ωm, the red lines for a resistive target (5000 Ωm) within a 10 Ωm background medium. b) subset of a) showing the results for the first 2000 measurements, with the grey dashed line showing the number of measurements comprising the standard survey design, and the red and blue dashed lines showing the relative resolution of a standard survey on a homogenous and resistive target, respectively.

813

814
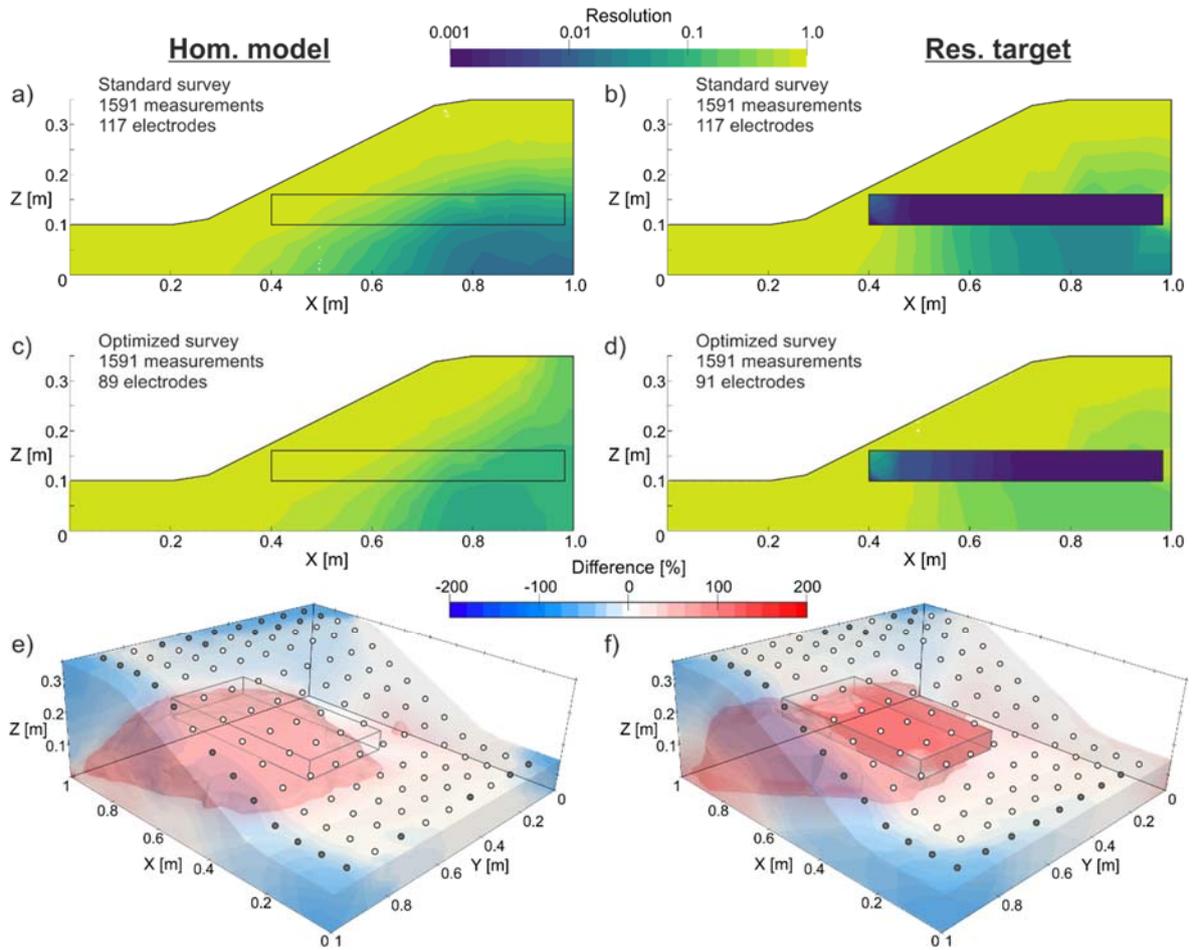
Figure 9 Model resolution at y = 0.5 m for the standard (a,b) and optimized survey designs (c,d), both applied to (a,c) a homogeneous (10 Ωm) medium, and (b,d) with the target being highly resistive (5000 Ωm). The resolution of this central model domain is clearly improved by the optimized survey designs. The bottom panel (e,f) shows the difference between the optimized and standard survey design, with an iso-volume indicating a 100 % improvement. White dots on the 3D plot indicate used electrode locations, while grey dots show electrode locations which are not used in the optimized design.

821

822
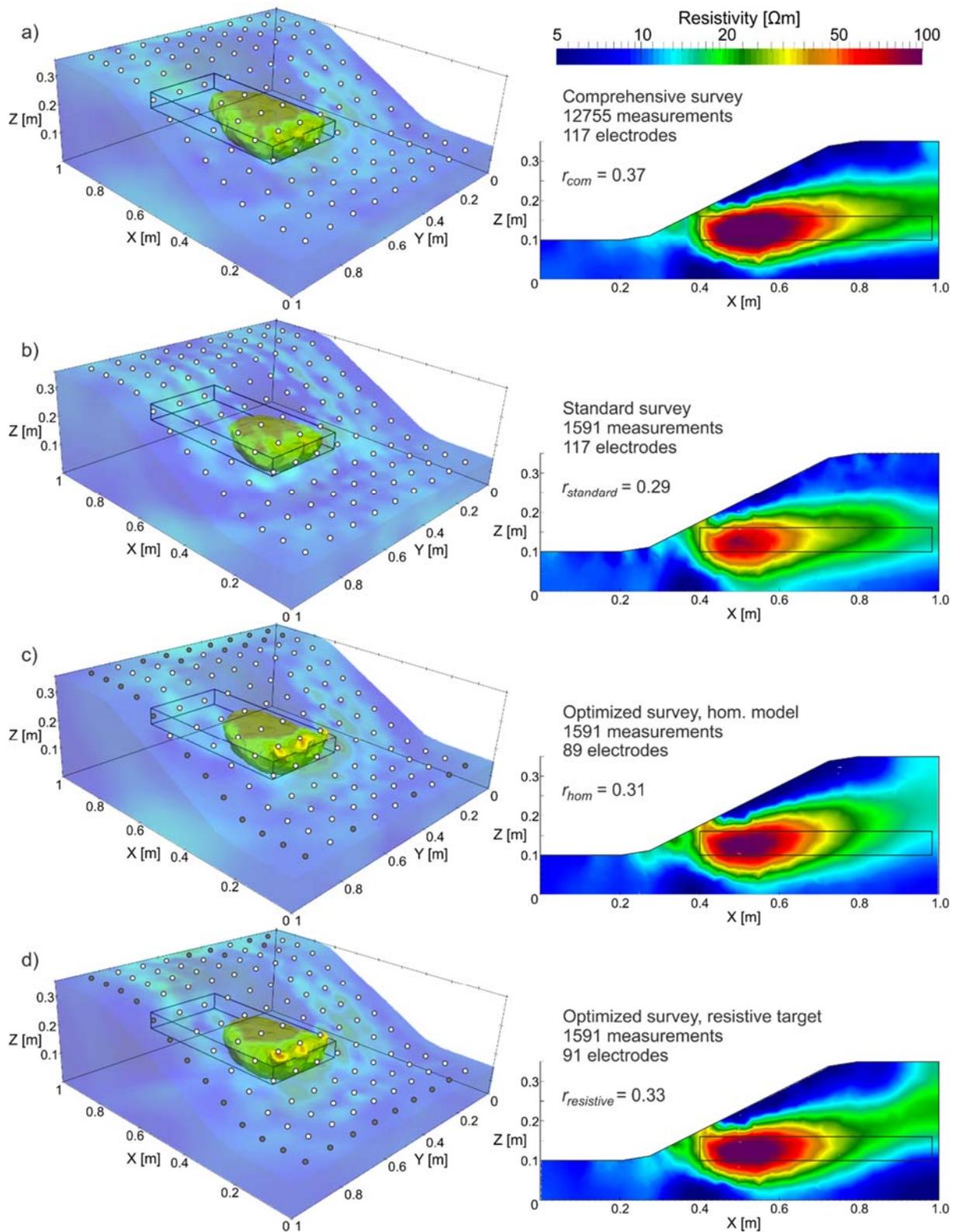
Figure 10 Inverted resistivity model for the 3D synthetic example; opaque iso-volumes indicates
resistivities ρ > 30 Ωm. a) results for the comprehensive survey, b) for the standard dipole-dipole and
Wenner-Schlumberger survey, and c)-d) for the optimized surveys calculated on a homogeneous model
and a resistive target, respectively. The slice of the right column is located centrally through the target
volume at y = 0.5 m. White dots on the 3D plots indicate used electrode locations, while grey dots show
electrode locations that are not used in the optimized design.

829
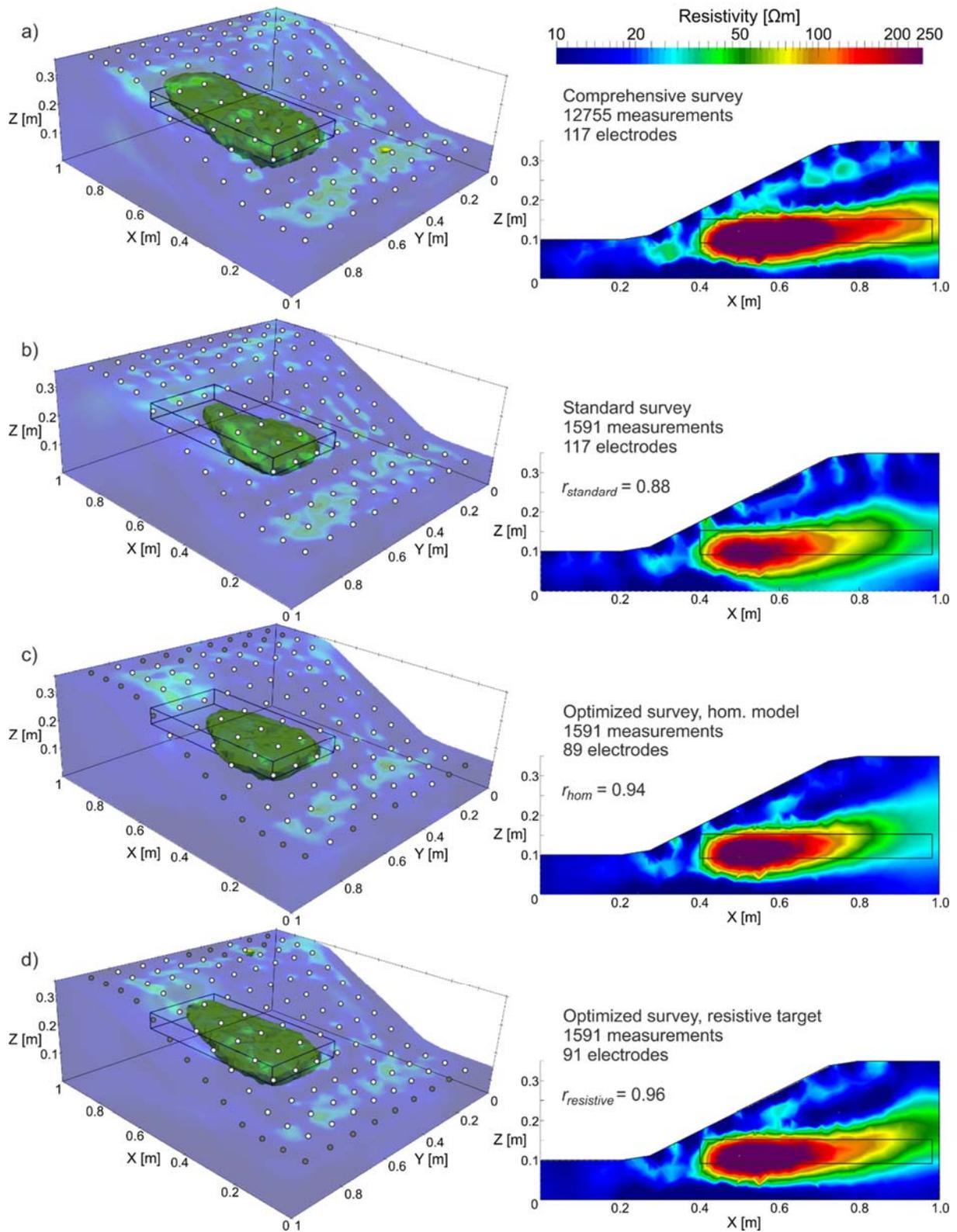
Figure 11 Inverted resistivity models of the laboratory data; opaque iso-volume indicates resistivities
of ρ > 60 Ωm; black box outlines the target volume. a) results for the comprehensive survey, b) for the
standard dipole-dipole, and Wenner-Schlumberger survey, and c)-d) for the optimized surveys
calculated on a homogeneous model and a resistive target, respectively. The slice of the right column
is located centrally through the target volume at y= 0.5 m. White dots on the 3D plots indicate used
electrode locations, while grey dots show electrode locations that are not used in the optimized design.